Density profile transition and high-energy electron transport in a magnetically expanding radio frequency plasma

Kazuma Emoto,[1,2,*] Kazunori Takahashi,[3] and Yoshinori Takao[1,†]

[1]*Division of Systems Research, Yokohama National University, Yokohama 240-8501, Japan*
[2]*Research Fellow, Japan Society for the Promotion of Science, Tokyo 102-0083, Japan*
[3]*Department of Electrical Engineering, Tohoku University, Sendai 980-8579, Japan*

Abstract

The density profile transition and high-energy electron transport in a magnetically expanding radio frequency (RF) plasma were investigated using particle-in-cell and Monte Carlo collision techniques, where both the plasma source and diffusion region were simulated self-consistently. The simulation results show that the density profile changes from center-peaked to bimodal plasma with increasing magnetic field strength, where bimodal plasma was observed in previous experiments. Then, the density profile transition is discussed with respect to ionization, electron temperature, and high-energy electron density. This indicates that the electrons were heated by the RF field and transported radially inward across the magnetic field lines. The moving distance of high-energy electrons is explained by an electron-neutral elastic collision. Therefore, the density formation depends on where the electrons are heated and how far the high-energy electrons are transported by an elastic collision, implying the longer existing time of high-energy electrons that move radially inward away from the RF antenna.

I INTRODUCTION

Magnetically expanding radio frequency (RF) plasmas have been widely used, for example, in the plasma processing of materials and plasma thrusters for space applications.[1–4] In magnetically expanding RF plasmas, high-density conics were observed in the diffusion region,[5–7] which were also mentioned as bimodal or hollow density profiles. Subsequent experiments showed that the magnetized electrons were heated near the RF antenna and transported mainly along the magnetic field lines that passed through the edge of the dielectric tube, generating peripheral high-temperature electrons and a conical density structure.[7–9] The relationship between the high-temperature electrons and magnetic field lines was investigated by changing the position of the RF antenna or the solenoid.[10,11] In addition, the effect of off-axis ionization due to the grad-B drift in the diffusion region has also been discussed.[12,13] In a numerical simulation, the power absorption density map inside the laboratory vacuum chamber was obtained using a plasma-wave model, indicating where the RF power was deposited in the plasma plume downstream of the source.[14] Several particle-in-cell (PIC) simulations in the diffusion region implied that the electrons were heated by the plasma instability.[15,16]

The downstream density profile, according to a model of magnetically expanding thrusters, affects the formation of internal plasma currents owing to $\boldsymbol{E}\times\boldsymbol{B}$ and diamagnetic drifts, as well as the resultant axial Lorentz force and the thruster performance.[17–19] Therefore, for improving the thruster performance, it is essential to understand the formation of density profiles. The hollow density profile implies that the high-energy electrons generated by peripheral RF heating are less likely to be transported to the radial-center region across the magnetic field lines. However, high-energy electron transport is not fully understood. To investigate the formation of the density profile with high-energy electron transport, particle simulations with self-consistent plasma generation are required, and several plasma dynamics must be analyzed: power absorption, ionization, high-energy electron confinement, and collisional particle transport.

Previous PIC simulations of magnetically expanding plasmas have focused on the diffusion region downstream of the plasma source.[15,16,20] However, both the plasma source and the diffusion region have to be simulated to accurately

*emoto-kazuma-vc@ynu.ac.jp
†takao@ynu.ac.jp

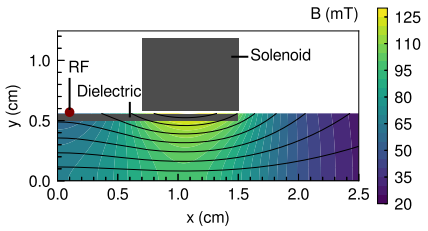

FIG. 1: A schematic of the two-dimensional calculation model. The thruster consists of a radio frequency (RF) antenna, a dielectric wall, and a solenoid coil. The color map depicts the magnetic field intensity at $I_B = 2.0\,\mathrm{kA}$. Solid black lines show the magnetic field lines.

understand the electron heating, the electron transport along and across the magnetic field lines, and the structural formation.

In this study, two-dimensional particle-in-cell simulations with Monte Carlo collisions (PIC-MCCs) were employed, and a magnetically expanding RF plasma was kinetically simulated, including the plasma source and diffusion region. The objective of this paper is to describe where high-energy electrons are generated by RF heating and how they are transported in magnetically expanding plasma. Here, only the inductive RF fields are considered to eliminate the complicated power absorption profile caused by the plasma-wave interaction, and only the magnetic field strength is modified. By fixing the discharge mode, the density profile formation depending on the magnetic field strength and high-energy electron transport can be discussed, where inductive heating and high-energy electron transport along the magnetic field lines have been implied in previous experiments.[11] Therefore, it is expected that the density profile formation can be reproduced even in a two-dimensional ICP model. As a result of the PIC-MCC simulations, the bimodal density profiles measured in previous experiments were generated by changing the magnetic field strength, implying that the inductive RF fields can reproduce the density transition independent of the plasma-wave interaction. In the remainder of this paper, the formation of high-density conics was also investigated from the perspective of electron heating and high-energy electron transport.

II NUMERICAL MODEL

Figure 1 shows the schematic of the calculation model. The calculation model is based on a previously used thruster with two open-source exits, in which space debris removal by bidirectional plasma ejection was demonstrated.[21] It should be noted that similar ion acceleration characteristics are obtained on the upstream and downstream sides of thrusters in both experiments and simulations,[22,23] implying that the bidirectional configuration has no effect on the essential physics of plasma expansion. The calculation area was assumed to be symmetric for the x- and y-axes. Symmetric and continuous boundary conditions were applied to the particle and field solvers on the x- and y-axes, which are described in detail later. The calculation area was set to approximately one-sixth of the scale of the experimental plasma source, reducing the calculation cost and avoiding central anomalies. In addition, the calculation area was set to a two-dimensional xy-plane with a $2.5\,\mathrm{cm} \times 0.56\,\mathrm{cm}$ region and had an infinite length in the z-direction, which was perpendicular to the xy-plane. The two-dimensional model can significantly reduce the calculation cost of solving Poisson's equation compared with the axisymmetric model because the fast Fourier transformation can be applied in both x- and y-directions.

The magnetically expanding RF plasma source consists of an RF antenna, solenoid coil, and dielectric wall, as shown in Fig. 1. The RF current induces electromagnetic fields and heats electrons. The lateral dielectric wall radially (y) confines low-energy electrons by the sheath.

For a charged particle, the equations of motion are as follows:

$$m\frac{d\boldsymbol{v}}{dt} = q(\boldsymbol{E}_{es} + \boldsymbol{E}_{em} + \boldsymbol{v} \times (\boldsymbol{B} + \boldsymbol{B}_{em})), \tag{1}$$

$$\boldsymbol{v} = \frac{d\boldsymbol{x}}{dt}, \tag{2}$$

where m is the particle mass; $\boldsymbol{v}$ is the particle velocity; t is the time; q is the particle charge; $\boldsymbol{x}$ is the position of the particle; $\boldsymbol{E}_{es}$ is the electrostatic field generated by the charged particles; $\boldsymbol{E}_{em}$ and $\boldsymbol{B}_{em}$ are the electromagnetic fields induced by the RF and plasma currents, respectively; and $\boldsymbol{B}$ is the magnetostatic field produced by the solenoid. The equations of motion are solved using the Boris method.[24] Particles incident to the outer boundaries (x = 2.5 cm and y = 0.56 cm) are assumed to disappear and thus excluded from the simulations. Particles incident on the dielectric are also excluded, but they accumulate as a surface charge on the dielectric, which is used in Poisson's equation for the electrostatic field $\boldsymbol{E}_{es}$. Particles incident on x- and y-axes were specularly reflected to ensure that the particle rotation was conserved. In the x-axis reflection, the velocity in the x-direction v_x is conserved, and the velocities in the y- and z-directions v_y and v_z are inverted. In the y-axis reflection, v_x is inverted, and v_y and v_z are conserved. Electron-neutral collisions were calculated using the null collisions method,[25] which is composed of elastic, excitation, and ionization collisions (see Table 2).

The surface charge density σ_s can be written as:

$$\sigma_s = \frac{e(N_{s,i} - N_{s,e})}{\Delta S}, \tag{3}$$

where e is the elementary charge; $N_{s,i}$ and $N_{s,e}$ are the accumulated numbers of single ions and electrons in the dielectric cell, respectively; and ΔS is the cell area. Then, the potential ϕ_t is calculated as:

$$\nabla^2 \phi_t = -\frac{e(n_i - n_e) + \sigma_s/\Delta y}{\varepsilon_0}, \tag{4}$$

where n_i and n_e are the ion and electron number densities, respectively; Δy is the cell size in the y-direction; and ε_0 is the vacuum permittivity. Equation (4) is solved using a fast Fourier transformation. Subsequently, the polarization charge σ_p is obtained from

$$\sigma_p = \frac{\chi \varepsilon_0 E_{es,t,\perp}}{\Delta y(1+\chi)}, \tag{5}$$

where χ is the susceptibility and $E_{es,t,\perp}$ is the perpendicular electrostatic field generated by ϕ_t. Here, it is assumed that the electrostatic field by ϕ_t is perpendicular to the dielectric surface and does not exist in vacuum. The susceptibility χ was set to 2.8, which is a typical value for glass tubes. The potential ϕ_p generated by σ_p was calculated as follows:

$$\nabla^2 \phi_p = -\frac{\sigma_p}{\varepsilon_0 \Delta y}. \tag{6}$$

Equation (6) can also be solved using fast Fourier transformation. Finally, the sum of the potentials ϕ is obtained from

$$\phi = \phi_t + \phi_p, \tag{7}$$

and the electrostatic field $\boldsymbol{E}_{es}$ is calculated as follows:

$$\boldsymbol{E}_{es} = -\nabla \phi. \tag{8}$$

Considering Gauss's law, the electrostatic field on the dielectric at y = 0.5 cm is obtained from

$$\nabla \cdot \boldsymbol{E}_{es} = \frac{e(n_i - n_e) + (\sigma_s + \sigma_p)/\Delta y}{\varepsilon_0}. \tag{9}$$

From Maxwell's equations, the electromagnetic field $\boldsymbol{E}_{em}$ induced by the RF antenna can be described as follows:

$$\left(\frac{\partial^2}{\partial x^2} + \frac{\partial^2}{\partial y^2} + \mu_0 \varepsilon_0 \omega^2 \right) \tilde{E}_{em} = i\omega \mu_0 \tilde{j}_p, \tag{10}$$

where μ_0 is the vacuum permeability; ω is the RF angular frequency; $\tilde{E}_{em}$ is the complex electric field; i is an imaginary unit; and $\tilde{j}_p$ is the complex plasma current density.[26,27] The complex plasma current $\tilde{j}_p$ is obtained from

$$\tilde{j}_p = -\frac{\sum qW v_z}{\Delta V} e^{i\Delta\psi}, \tag{11}$$

where W is the particle weight; ΔV is the cell volume; v_z is the particle velocity in the z-direction; and $\Delta\psi$ is the phase difference between the RF and plasma currents.[26,27] The electromagnetic field $\boldsymbol{B}_{em}$ is also calculated from Faraday's law.

The calculation area for the RF field was set to 1.5 cm × 0.5 cm only for the plasma source. As boundary conditions, we set $\tilde{E}_{em} = 0$ on the x-axis and $\partial\tilde{E}_{em}/\partial x = 0$ on the y-axis. The electric fields $\tilde{E}_{em}$ on the dielectric at $y = 0.5$ cm and the right boundary at $x = 1.5$ cm were calculated using Biot-Savart's law and Faraday's law.[28] Note that the RF discharge model employed in this study considers only the inductively coupled mode and does not contain capacitively coupled or wave modes.

The magnetostatic field produced by a solenoid $\boldsymbol{B}$ was calculated using Maxwell's equations. The calculation area for the magnetostatic field was set as 25 cm × 5.6 cm to ignore the outer boundary effects. $A_z = 0$ on the x-axis and the outer boundaries, and $\partial A_z/\partial x = 0$ on the y-axis are assumed as boundary conditions.

Table 1 summarizes the calculation conditions used in this study. Xe^+ and e^- were employed as charged particles, and multiply-charged ions were not considered for simplicity. The time steps of the charged particles are set to 125 ps for ions (1/100 RF period) and 3.57 ps for electrons (1/35 time step for ions). Electron-neutral collisions consist of elastic, excitation, and ionization collisions. The cross-sections employed in the simulations are summarized in Table 2 and plotted in Fig. 2. The neutral density and temperature were assumed to be uniform, 3×10^{19} m^{-3} and 300 K, respectively, corresponding to a pressure of 83 mPa. The RF frequency was set to 80 MHz under the same conditions as those in our previous simulations.[29,30] The RF current is controlled to keep the power absorption at 3.5 W. In this study, the power absorption of the plasma was defined as the sum of the changes in the particle kinetic energies.[26] The calculation area is divided by cells of 50 µm × 50 µm to satisfy the limitation of Debye length. The initial ions and electrons were uniformly placed in the calculation area, and the initial number of particles per cell was set to 100. The particle weight was 2.5×10^6. A steady state was obtained after 5,000 RF cycles (62.5 µs) from the beginning of the simulations, and the electron number density was within ±5%. Then, the simulation results were averaged over 37.5 µs from the steady state, which is equivalent to 3,000 RF periods. To investigate the dependency on the magnetic field strength, three solenoid currents of 0.1, 0.4, and 2.0 kA were employed while unchanging the structure of the field lines. The magnetic field strength and magnetic field lines at 2.0 kA are shown in Fig. 1.

Note that the neutral pressure and the size of the vacuum chamber are not expected to affect the density profile formation because in many experiments with various conditions, a bimodal density profile has been observed.[6,31] However, the density profile was modified by changing the magnetic field strength;[32] therefore, only the magnetic field strength is changed in this study.

III RESULTS AND DISCUSSION

Figure 3 shows x-y profiles of the electron number density n_e for the three solenoid currents of 0.1, 0.4, and 2.0 kA. It can be seen that n_e increases as the solenoid current increases, owing to electron confinement by the magnetic field. In addition, the radial (y) density profiles were significantly affected by the magnetic field strength. To compare the y profile of the density in greater detail, Fig. 4 shows y profiles of the electron number density n_e for three solenoid currents of 0.1, 0.4, and 2.0 kA at $x = 0$ and 1.5 cm. The densities were maximized at $y = 0$ and decreased along the y-axis for the 0.1 and 0.4 kA cases. The density profiles correspond to the center-peaked plasmas due to the symmetric calculation model for x-axis. However, for the 2.0 kA case, the density is maximized at $y = 0.1$ cm, and the hollow region is generated around $y = 0$. This density profile is bimodal plasma owing to the symmetry, which is consistent with the previous experimental results.[5–10,12,13]

Figure 5 shows x-y profiles of the electron temperature T_e for the three solenoid currents of 0.1, 0.4, and 2.0 kA. Figure 6 also shows y profiles of the electron temperature T_e for three solenoid currents of 0.1, 0.4, and 2.0 kA at $x = 0$

TABLE. 1: Calculation condition.

Parameters	Values
Particles	Xe^+ and e^-
Time step for ions	125 ps (1/100 RF period)
Time step for electrons	3.57 ps (1/35 time step for ions)
Neutral density	3×10^{19} m^{-3}
Neutral temperature	300 K
RF frequency	80 MHz
Power absorption	3.5 W
Cell size	50 µm × 50 µm

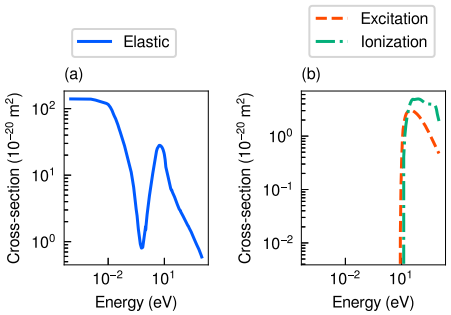

FIG. 2: Xenon cross-sections employed in the simulations: (a) elastic and (b) excitation and ionization.

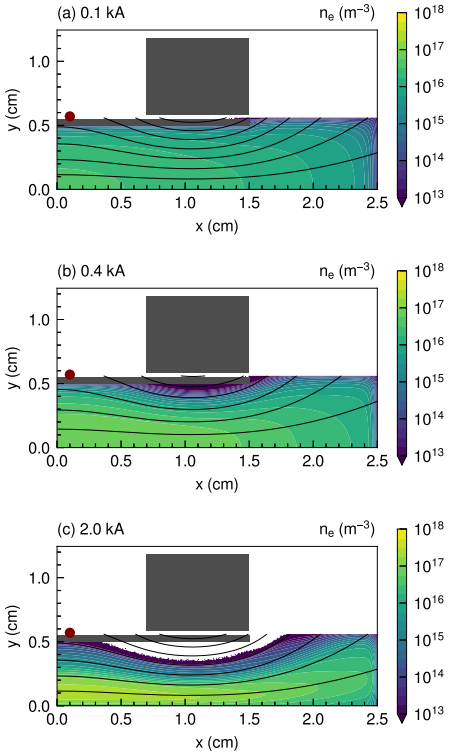

FIG. 3: x-y profiles of the electron number density n_e for the three solenoid currents of (a) 0.1, (b) 0.4, and (c) 2.0 kA. Solid black lines show the magnetic field lines.

TABLE. 2: Xenon cross-sections employed in the simulations.

Reactions	References
$Xe + e^- \rightarrow Xe + e^-$	[33]Heer, et al.
$Xe + e^- \rightarrow Xe^* + e^-$	[34]Hayashi, et al.
$Xe + e^- \rightarrow Xe^+ + 2\,e^-$	[35]Rapp, et al.

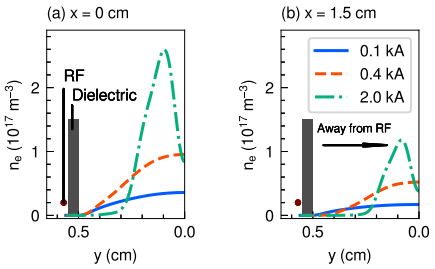

FIG. 4: y profiles of the electron number density n_e for the three solenoid currents of 0.1, 0.4, and 2.0 kA at (a) $x = 0$ and (b) $x = 1.5$ cm.

and $x = 1.5$ cm. T_e was calculated using

$$T_e = \frac{m_e N_e}{3k_B(N_e - 1)}\left(\frac{\sum \boldsymbol{v}_e^2}{N_e} - \boldsymbol{u}_e^2\right), \tag{12}$$

where m_e is the electron mass; N_e is the number of electrons; k_B is Boltzmann's constant; $\boldsymbol{v}_e$ is the electron particle velocity; and $\boldsymbol{u}_e$ is the electron flow velocity. As shown in Figs. 5 and 6, the electron temperature is relatively high in the peripheral region near the dielectric and low in the central region because the electrons are well heated near the RF antenna owing to the inductively coupled mode. For strong magnetic fields of 0.4 and 2.0 kA, a similar electron temperature is distributed along the magnetic field lines, indicating electron confinement by the magnetic field.

The mean free path l of the high-temperature electrons is estimated from $l = (n_n\sigma)^{-1}$, where n_n represents the neutral density and σ represents the cross section. When σ is approximately assumed to be 1×10^{-19} m^2 from Fig. 2, l becomes 33.3 cm using the calculation condition $n_n = 3 \times 10^{19}$ m^{-3} (see Table 1). Therefore, l is sufficiently larger than the plasma source size, and most electrons move along the magnetic field lines without collisions. Because the electrons are repelled by the potential drop in the diffusion region or the magnetic mirror at the magnetic throat, they are heated by the inductive field under the RF antenna, and a high-temperature region is produced, as shown in Fig. 5.

The ionization rate was analyzed in the simulations to investigate the formation of the density profiles. Figure 7 shows the x-y profiles of the ionization rate G_{iz} for three solenoid currents of 0.1, 0.4, and 2.0 kA. The y profiles of the ionization rate G_{iz} at those solenoid currents at $x = 0$ and $x = 1.5$ cm are also shown. From Figs. 3, 4, 7, and 8, it is observed that the region with a high ionization rate corresponds to the high-density region. Thus, most electrons generated through ionization move mainly along the magnetic field lines and are transported across the magnetic field lines to a less extent.

The electron Larmor radius was estimated using the electron temperature T_e shown in Fig.5 and the magnetic field strength B. The electron thermal velocity is employed, and the electron Larmor radius can be expressed as

$$r_L = \sqrt{\frac{8m_e T_e}{e\pi B^2}}. \tag{13}$$

Figure 9 shows the x-y profiles of the electron Larmor radius r_L for three solenoid currents: 0.1, 0.4, and 2.0 kA. The electron Larmor radius r_L at 0.1 kA is 1–5 mm, which is comparable to the thruster height of 0.5 cm. However, r_L at 0.4 and 2.0 kA is sufficiently smaller than the thruster size, indicating electron magnetization.

Sufficiently high-energy electrons are required for ionization. In this study, the simulations were performed considering xenon gas, and an energy of 12.1 eV or more was required to ionize neutrals. Here, the number density of electrons with

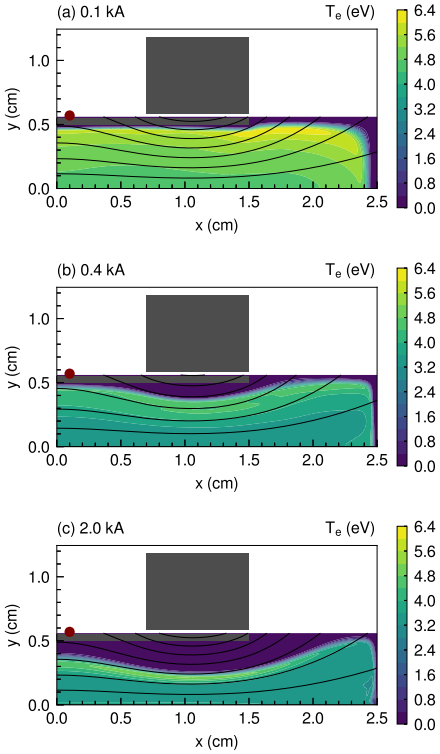

FIG. 5: x-y profiles of the electron temperature T_e for the three solenoid currents of (a) 0.1, (b) 0.4, and (c) 2.0 kA. Solid black lines show the magnetic field lines.

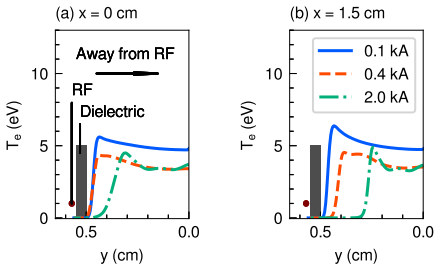

FIG. 6: y profiles of the electron temperature T_e for the three solenoid currents of 0.1, 0.4, and 2.0 kA at (a) x = 0 and (b) x = 1.5 cm.

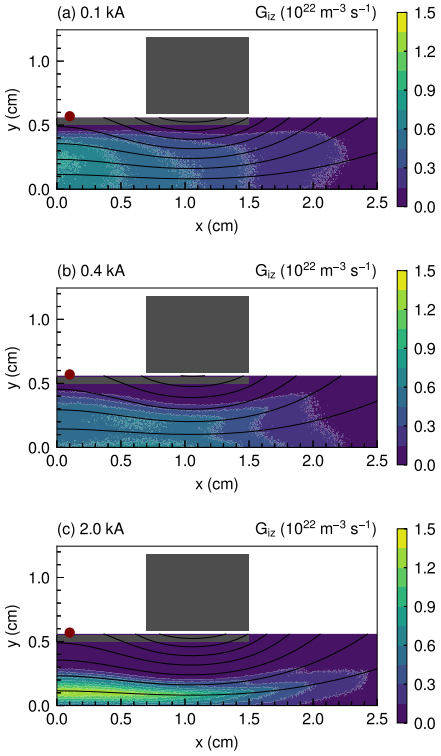

FIG. 7: x-y profiles of the ionization rate G_{iz} for the three solenoid currents of (a) 0.1, (b) 0.4, and (c) 2.0 kA. Solid black lines show the magnetic field lines.

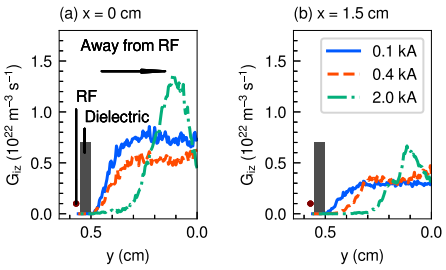

FIG. 8: y profiles of the ionization rate G_{iz} for the three solenoid currents of 0.1, 0.4, and 2.0 kA at (a) $x = 0$ and (b) $x = 1.5$ cm.

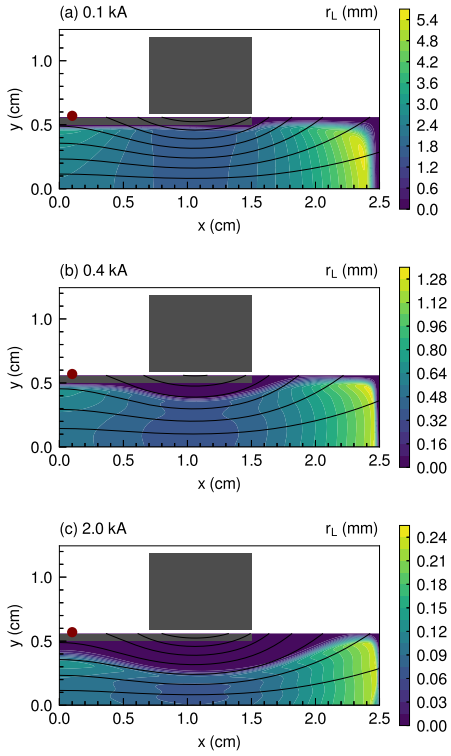

FIG. 9: x-y profiles of the electron Larmor radius r_L for the three solenoid currents of (a) 0.1, (b) 0.4, and (c) 2.0 kA. Solid black lines show the magnetic field lines.

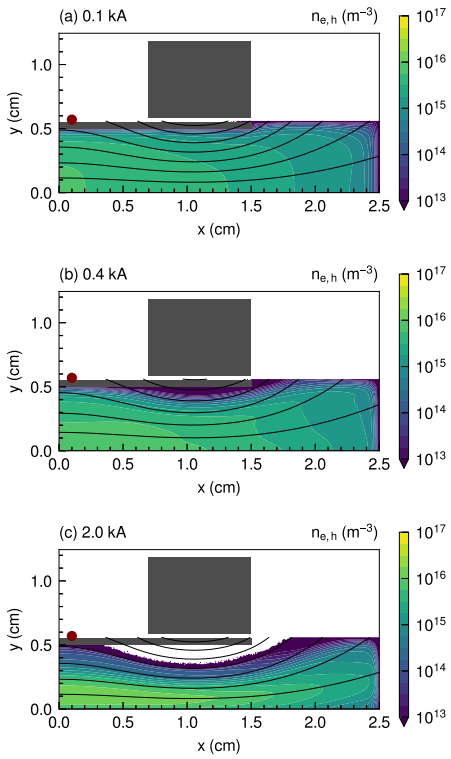

FIG. 10: x-y profiles of the high-energy electron number density $n_{e,h}$ for the three solenoid currents of (a) 0.1, (b) 0.4, and (c) 2.0 kA. Solid black lines show the magnetic field lines.

energies above 12.1 eV was extracted from n_e shown in Fig. 3. Figure 10 shows the x-y profiles of the high-energy electron number density $n_{e,h}$ for three solenoid currents: 0.1, 0.4, and 2.0 kA. The y profiles of the high-energy electron number density $n_{e,h}$ for those currents at $x = 0$ and $x = 1.5$ cm are also shown. From Figs. 7 and 10, it can be confirmed that $n_{e,h}$ is high when the ionization rate is high. Therefore, the presence of high-energy electrons determines the probability of ionization in the plasma source.

Figure 12 shows the x-y profiles of the high-energy electron ratio $n_{e,h}/n_e$ for three solenoid currents: 0.1, 0.4, and 2.0 kA. The y profiles of the high-energy electron ratio $n_{e,h}/n_e$ for those at $x = 0$ and $x = 1.5$ cm are also shown. There are clear differences between the high-energy electron ratio and density profiles. The high-energy electron ratio increases in the outer region ($y > 0.3$ cm), whereas the high-energy electron density increases in the inner region ($y < 0.3$ cm). Additionally, the profiles of the high-energy electron ratio were roughly consistent with those of the electron temperature, as shown in Fig. 5. Thus, the high-energy electron density profiles directly affect the ionization rate and density profile formation.

For ionization, electrons must be heated to a sufficient energy, which should be greater than the ionization energy of 12.1 eV. In magnetically expanding RF plasma, energy is supplied only from the RF field, and the power absorption under the RF antenna is expected to be high in the presence of inductive fields. Figure 14 shows x-y profiles of the power absorption per electron $p_{abs,e}$ for three solenoid currents (0.1, 0.4, and 2.0 kA), where $p_{abs,e}$ is calculated from the change in the electron kinetic energy. As seen in Fig. 14, $p_{abs,e}$ is high in the peripheral region near the dielectric, indicating

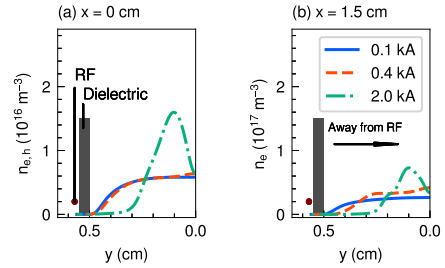

FIG. 11: y profiles of the high-energy electron number density $n_{e,h}$ for the three solenoid currents of 0.1, 0.4, and 2.0 kA at (a) $x = 0$ and (b) $x = 1.5$ cm.

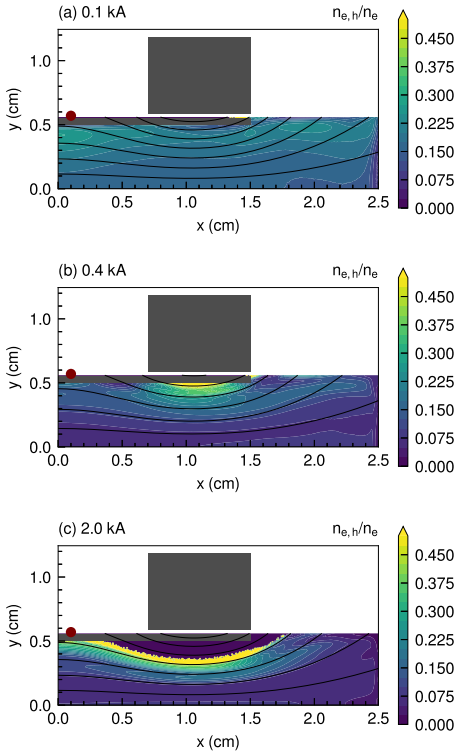

FIG. 12: x-y profiles of the high-energy electron ratio $n_{e,h}/n_e$ for the three solenoid currents of (a) 0.1, (b) 0.4, and (c) 2.0 kA. Solid black lines show the magnetic field lines.

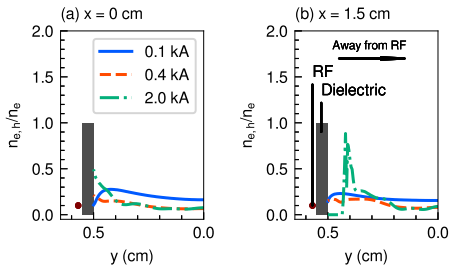

FIG. 13: y profiles of the high-energy electron ratio $n_{e,h}/n_e$ for the three solenoid currents of 0.1, 0.4, and 2.0 kA at (a) x = 0 and (b) x = 1.5 cm.

inductively coupled heating by the RF field. In addition, the large positive values of $p_{abs,e}$ appear to be very similar to those obtained in previous studies,[6–10,12] which have discussed the possible interpretations of electron heating by inductive fields. The results obtained at 0.4 and 2.0 kA in this study indicate that the electrons are energized at the axial location of the solenoid rather than at the RF antenna. Although the detailed energizing process is not yet understood, this result might explain the non-local generation of plasma in the convergent magnetic field.[11]

The electrons heated in the peripheral region mainly moved along the magnetic field lines; therefore, the electron temperature was high in the peripheral region, as shown in Fig. 5. However, the high-temperature region shown in Fig. 5 is different from that in the high-energy-density region shown in Fig. 10. This implies that high-energy electrons heated by the RF field are also transported to the inner region (negative y-direction) across the magnetic field lines.

Figure 15 shows x-y profiles of the high-temperature and high-energy-density lines for three solenoid currents (0.1, 0.4, and 2.0 kA), where the high-temperature and high-energy-density lines are extracted by taking the maximum values in the y-profiles from Figs. 5 and 10. The calculation model was symmetric with $y = 0$. On average, high-energy electrons were expected to be transported from the high-temperature line (solid blue line) to the high-energy-density line (dashed orange line). Because the two-dimensional calculation model does not have an electric field in the z-direction, $\boldsymbol{E} \times \boldsymbol{B}$ drifts in the xy-plane do not occur. In addition, the cyclotron frequency ω_c is sufficiently larger than the collision frequency ν, where ω_c and ν are roughly estimated to be 10^9 Hz and 10^5 Hz, respectively. Therefore, only electron-neutral elastic collisions can transport high-energy electrons across magnetic field lines while conserving their energies. Here, an electron exists in the width of $2r_L$ in the direction perpendicular to the magnetic field, and an elastic collision can shift the guiding center by $2r_L$, as shown in Fig. 15(d). Thus, the maximum probable moving distance from an elastic collision is estimated to be $4r_L$.

To estimate the maximum probable moving distance, the Larmor radius was calculated using the magnetic field strength on the high-temperature line and the minimum required energy of 12.1 eV for high-energy electrons. The green regions in Fig. 15 correspond to a distance of $4r_L$ from the high-temperature line (solid blue line) in the negative y-direction. A high-energy electron on the high-temperature line can be transported in the direction along the green arrow by an elastic collision. Notably, the negative y-direction (not accurately perpendicular to the magnetic field) and the magnetic properties on the high-temperature line are considered for this estimation.

At 0.1 kA, the $4r_L$ region occupies almost the entire calculation area ($-0.5\,\text{cm} < y < 0.5\,\text{cm}$), indicating that high-energy electrons on the high-temperature line can be transported across the high-energy-density line by an elastic collision. However, at 0.4 kA, the $4r_L$ region occupies approximately the upper half region ($0 < y < 0.5$ cm). Although high-energy electrons on the high-temperature line can be transported around $y = 0$ by an elastic collision, fewer of them are transported across $y = 0$. Finally, at 2.0 kA, the $4r_L$ region is relatively small and does not reach approximately $y = 0$. Transporting high-energy electrons on the high-temperature line to the region around $y = 0$ is difficult; therefore, a hollow density profile is obtained, as shown in Fig. 3(c).

The distance $4r_L$ increases in the downstream region because the magnetic field strength rapidly decreases. Therefore, high-energy electrons can move over long distances in the downstream region. The high-temperature and high-energy-density regions have variations around each maximum line, and a minimum ionization energy of 12.1 eV is assumed in this estimation. Because of the limitations of this estimation, it is reasonable that the high-energy-density lines are roughly

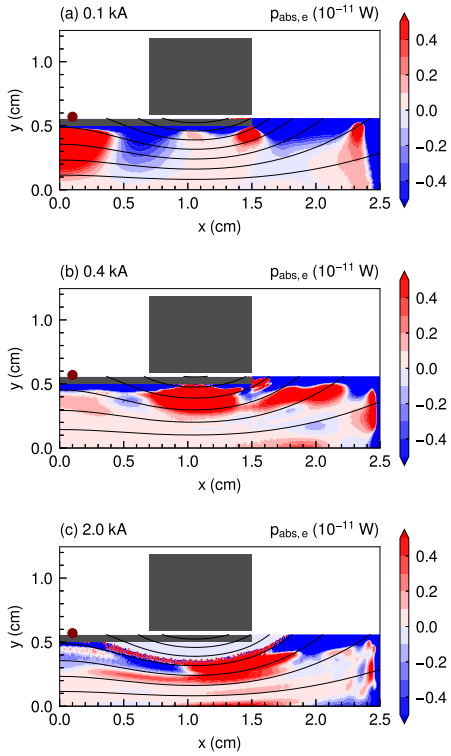

FIG. 14: x-y profiles of the electron power absorption density $p_{abs,e}$ for the three solenoid currents of (a) 0.1, (b) 0.4, and (c) 2.0 kA. Solid black lines show the magnetic field lines.

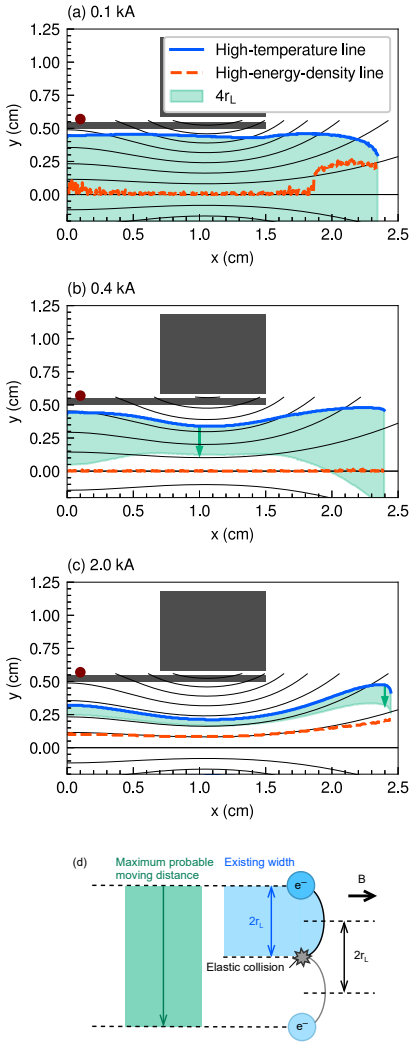

FIG. 15: x-y profiles of the high-temperature and high-energy-density lines for the three solenoid currents of (a) 0.1, (b) 0.4, and (c) 2.0 kA. The elastic collisional moving distance $4r_L$ from the high-temperature line is also plotted. Solid black lines show the magnetic field lines. (d) A schematic of the electron exiting width in the magnetic field and the maximum probable moving distance by an elastic collision.

determined by the collisional moving distance from the high-temperature lines.

To explain why the high-energy electrons are transported in the negative y-direction, two patterns of high-energy electrons are assumed: (i) high-energy electrons that do not collide with neutrals in the high-temperature region and remain heated under the RF antenna, and (ii) high-energy electrons that collide with neutrals in the high-temperature region and move in the negative y-direction away from the RF antenna. In pattern (i), the high-energy electrons are heated under the RF antenna because of magnetic confinement, even though the electrons already have enough energy to ionize a neutral. The energy of the electrons (i) continues to increase and is likely to be lost to the wall by overcoming the sheath potential. However, in pattern (ii), the high-energy electrons move in the negative y-direction after being heated by the RF field. Although their energies are less likely to increase by RF heating, the energies are sufficient to ionize a neutral, and high-energy electrons away from the RF antenna can be prevented from overheating. Therefore, high-energy electron energies (ii) are unlikely to exceed the sheath potential and are less likely to be lost to the wall. Consequently, the number of high-energy electrons increased. The high-energy electrons mentioned in (ii) are expected to have longer existing times than those in (i) and increase the ionization probability. Note that a high temperature implies a high ratio of high-energy electrons, whereas a high-energy electron density indicates a large number of high-energy electrons.

The least heated region is the center of the plasma source (on the x-axis around $y = 0$ in this study), which corresponds to the center-peaked plasma for the weak magnetic field strength in Figs. 3(a) and 3(b). Increasing the intensity of the magnetic field restricts the radial electron transport and is expected to produce the bimodal plasma profile shown in Fig. 3(c). The density profile transition observed in magnetically expanding RF plasmas can be explained by the extent to which high-energy electrons are transported by an elastic collision.

Previous studies have shown that the density profile transition depends on the discharge mode and power absorption.[36,37] However, PIC-MCC simulations in this study demonstrates that the significant change in the radial density profile depends on the magnetic field strength and the high-energy electron transport. As mentioned in Sec. II, only inductive mode discharge is considered, and the wave effect is artificially eliminated. Here, the center-peaked profiles are detected for the 0.1 and 0.4 kA cases, whereas the bimodal density profile is formed by increasing the magnetic field strength to 2.0 kA. Therefore, the density profile formation depends not only on the discharge mode and power absorption but also on the magnetic field strength and the radially high-energy electron transport across the magnetic field lines.

The Dirichlet boundary condition was assumed to be $x = 2.5$ cm in the simulations, and the sheath was generated near the boundary. Thus, the electrons reflected by the sheath may move to the inner magnetic field lines. This effect can be eliminated by employing an open boundary condition, but numerical convergence is an issue to be addressed for obtaining a steady plasma. To fully understand high-energy electron transport, further numerical investigation with an open boundary condition is required.

IV CONCLUSION

Two-dimensional PIC-MCC simulations for magnetically expanding RF plasma were conducted to investigate the density profile transition and high-energy electron transport. The density profile changed from center-peaked to bimodal plasma with increasing magnetic field strength, and bimodal density profiles were reproduced in the simulation, as observed in previous experiments. The density profile transition was discussed with respect to the ionization, electron temperature, and high-energy electron density. The high-temperature region was different from the high-energy-density region, indicating that high-energy electrons were generated in the peripheral region and transported to the high-energy-density region across the magnetic field lines by electron-neutral elastic collisions. The high-energy-density line was determined based on the moving distance of the high-energy electrons by an elastic collision, whereby a hollow density region was generated for the strong magnetic field condition. The density profile formation depends on the regions where the electrons are heated and how far the high-energy electrons are transported by an elastic collision. This implies that high-energy electrons that move radially inward away from the RF antenna exist for a longer time.

The density profile transition is reproduced in the two-dimensional ICP model without wave effects, demonstrating the dependence of the magnetic field strength and high-energy electron transport across the magnetic field lines on the density profile formation. These numerical results support the conclusion derived in previous experiments, where inductive heating and high-energy electron confinement produced a bimodal density profile.

Although a bimodal density profile was observed in the two-dimensional ICP model, the plasma instabilities and anomalous transport reproduced in the three-dimensional model may have a relevant role in the density profile formation. Recently, electron detachment due to instabilities was discussed;[38–40] this detachment might also affect the density profile formation. present PIC-MCC simulations cannot treat three-dimensional models because of the calculation cost, but these

effects will be analyzed in the future.

AUTHOR DECLARATIONS

Conflict of Interest

The authors have no conflicts to disclose

ACKNOWLEDGEMENT

This work was partly supported by JSPS KAKENHI Grant Numbers JP21J15345 and JP19H00663 and JST FOREST Program (Grant Number JPMJFR212A, Japan). The computer simulation was performed on the A-KDK computer system at Research Institute for Sustainable Humanosphere, Kyoto University. This research is partially supported by Initiative on Promotion of Supercomputing for Young or Women Researchers, Information Technology Center, The University of Tokyo. This work used computational resources of Fugaku provided by RIKEN Center for Computational Science through the HPCI System Research Project (Project ID: hp210329).

DATA AVAILABILITY

The data that support the findings of this study are available from the corresponding authors upon reasonable request.

References

[1]P. Chabert, N. Proust, J. Perrin, and R. Boswell, Appl. Phys. Lett. **76**, 2310 (2000).

[2]K. Hanaoka and K. Takahashi, AIP Adv. **11**, 025013 (2021).

[3]C. Charles, J. Phys. D: Appl. Phys. **42**, 163001 (2009).

[4]K. Takahashi, Rev. Mod. Plasma Phys. **3**, 3 (2019).

[5]W. Cox, R. Hawkins, C. Charles, and R. Boswell, IEEE Trans. Plasma Sci. **36**, 1386 (2008).

[6]C. Charles, Applied Physics Letters **96**, 051502 (2010).

[7]K. Takahashi, C. Charles, R. Boswell, W. Cox, and R. Hatakeyama, Appl. Phys. Lett. **94**, 191503 (2009).

[8]Y. Zhang, C. Charles, and R. Boswell, Phys. Plasmas **23**, 083515 (2016).

[9]N. Gulbrandsen and Å. Fredriksen, Front. Phys. **5**, 2 (2017).

[10]K. Takahashi, H. Akahoshi, C. Charles, R. Boswell, and A. Ando, Phys. Plasmas **24**, 084503 (2017).

[11]A. Bennet, C. Charles, and R. Boswell, Phys. Plasmas **26**, 072107 (2019).

[12]S. Ghosh, S. Yadav, K. Barada, P. Chattopadhyay, J. Ghosh, R. Pal, and D. Bora, Phys. Plasmas **24**, 020703 (2017).

[13]S. Yadav, S. Ghosh, S. Bose, K. Barada, R. Pal, and P. K. Chattopadhyay, Phys. Plasmas **25**, 043518 (2018).

[14]B. Tian, M. Merino, and E. Ahedo, Plasma Sources Sci. Technol. **27**, 114003 (2018).

[15]S. Rao and N. Singh, Phys. Plasmas **19**, 093507 (2012).

[16]N. Singh, S. Rao, and P. Ranganath, Phys. Plasmas **20**, 032111 (2013).

[17]E. Ahedo and M. Merino, Phys. Plasmas **17**, 073501 (2010).

[18]K. Takahashi, T. Lafleur, C. Charles, P. Alexander, and R. W. Boswell, Phys. Rev. Lett. **107**, 235001 (2011).

[19]K. Takahashi, C. Charles, and R. W. Boswell, Phys. Rev. Lett. **110**, 195003 (2013).

[20]Z. Chen, Y. Wang, H. Tang, J. Ren, M. Li, P. Wu, and J. Cao, Plasma Sources Sci. Technol. **30**, 105012 (2021).

[21]K. Takahashi, C. Charles, R. Boswell, and A. Ando, Sci. Rep. **8**, 14417 (2018).

[22]Y. Zhang, C. Charles, and R. Boswell, Appl. Phys. Lett. **108**, 104101 (2016).

[23]V. Saini and R. Ganesh, J. Plasma Phys. **88**, 905880203 (2022).
[24]C. Birdsall and A. Langdon, *Plasma physics via computer simulation* (1991).
[25]V. Vahedi and M. Surendra, Comput. Phys. Comm. **87**, 179 (1995).
[26]Y. Takao, N. Kusaba, K. Eriguchi, and K. Ono, J. Appl. Phys. **108**, 093309 (2010).
[27]Y. Takao, K. Eriguchi, and K. Ono, J. Appl. Phys. **112**, 093306 (2012).
[28]K. Emoto, K. Takahashi, and Y. Takao, Plasma Sources Sci. Technol. **30**, 115016 (2021).
[29]Y. Takao and K. Takahashi, Phys. Plasmas **22**, 113509 (2015).
[30]K. Takase, K. Takahashi, and Y. Takao, Phys. Plasmas **25**, 023507 (2018).
[31]K. Takahashi, Sci. Rep. **11**, 2768 (2021).
[32]K. Takahashi, A. Chiba, A. Komuro, and A. Ando, Plasma Sources Sci. Technol. **25**, 055011 (2016).
[33]F. J. de Heer, R. H. J. Jansen, and W. van der Kaay, J. Phys. B: At. Mol. Phys. **12**, 979 (1979).
[34]M. T. Hayashi, J. Phys. D: Appl. Phys. **16**, 581 (1983).
[35]D. Rapp and P. Englander-Golden, J. Chem. Phys. **43**, 1464 (1965).
[36]A. Degeling, C. Jung, R. Boswell, and A. Ellingboe, Phys. Plasmas **3**, 2788 (1996).
[37]C. M. Franck, O. Grulke, and T. Klinger, Phys. Plasmas **10**, 323 (2003).
[38]S. Hepner, B. Wachs, and B. Jorns, Appl. Phys. Lett. **116**, 263502 (2020).
[39]K. Takahashi, C. Charles, and R. Boswell, Bulletin of the American Physical Society (2022).
[40]K. Takahashi, C. Charles, and R. Boswell, Sci. Rep., to be published (2022).

Physics of Plasmas

PLEASE CITE THIS ARTICLE AS DOI: 10.1063/5.0126901